Research Square

Preprints are preliminary reports that have not undergone peer review.
They should not be considered conclusive, used to inform clinical practice,
or referenced by the media as validated information.

An ROS-responsive photosynthetic biosystem disrupts the infectious-inflammatory-hypoxic cycle in pneumonia

Lili Huang

llhuang@bit.edu.cn

Beijing Institute of Technology https://orcid.org/0000-0002-0007-4427

Zewei Yan

Inner Mongolia Normal University

Kunpeng Li

Beijing Institute of Technology

Wenfeng Xu

Beijing Hospital; National Center of Gerontology

Ruiqi Ming

South China Normal University

Zhongjie Wang

Beijing Institute of Technology

Chuyu Li

Beijing Institute of Technology

Hanlin Chen

Beijing Institute of Technology

Shujun Liu

Beijing Institute of Technology

Yuantian Jing

Beijing Institute of Technology

Rui Zhang

Beijing Institute of Technology

Yingjie Shi

China Medical University

Yimei Pan

Beijing Institute of Technology

Jiajie Tian

Beijing Institute of Technology

Pengfei Jin

Beijing Hospital; National Center of Gerontology

Jinghuan Li

Inner Mongolia Normal University

Article

Keywords:

Posted Date: October 29th, 2026

DOI: https://doi.org/10.21203/rs.3.rs-11240743/v1

License: This work is licensed under a Creative Commons Attribution 4.0 International License.
Read Full License

Additional Declarations: There is **NO** Competing Interest.

Abstract

Acute lung injury (ALI) is sustained by a self-reinforcing cycle of inflammation, oxidative stress and hypoxia that current therapies cannot fully disrupt. To break this cycle, we engineered *Haematococcus pluvialis* (Hae) with chemiluminescent peroxyoxalate (CPPO) and fluorophore (Cy5) to construct a ROS-responsive photosynthetic biosystem (Hae@CC) for ALI therapy. Upon nebulization, excess H2O2 at the lesion triggers chemiluminescence (CL), which activates Cy5 through resonance energy transfer and drives endogenous Hae photosynthesis to produce oxygen (O_2) and the antioxidant astaxanthin (AST). In both lipopolysaccharide (LPS)- and bacteria-induced murine ALI models, aerosolized Hae@CC reduces bacterial load, alleviates pulmonary oedema and inflammation, promotes M2-biased macrophage polarization, enhances angiogenesis and improves pulmonary function, outperforming dexamethasone across multiple endpoints, with no appreciable toxicity in vivo. By correcting local hypoxia and redox imbalance, this biosystem resets the alveolar microenvironment, establishing that restoring homeostatic control, rather than blocking individual mediators, resolves inflammatory tissue injury.

Introduction

Acute lung injury (ALI) and its most severe form, the acute respiratory distress syndrome (ARDS), remain leading causes of death in critically ill patients, driven by a self-perpetuating cycle of inflammation, oxidative stress and hypoxia[1–4]. In the lungs, both infectious (e.g., bacterial pathogens) and non-infectious (e.g., trauma, aspiration) stimuli initiate excessive immune responses. Alveolar macrophages polarize to the pro-inflammatory M1 phenotype, and infiltrating neutrophils and monocytes generate overwhelming amounts of reactive oxygen species (ROS), damaging the pulmonary epithelium and endothelium[5–8]. This oxidative injury disrupts the alveolar-capillary barrier, leading to tissue hypoxia[9,10], conversely, hypoxia stabilizes HIF-1α, which further amplifies both inflammatory gene expression and ROS generation, creating a self-reinforcing loop[11,12]. Thus, breaking this triad is essential for effective ALI therapy.

Current clinical management of ALI/ARDS, including systemic corticosteroids, mechanical ventilation, and antibiotics, provides life-sustaining support but does not break the inflammation-oxidative stress-hypoxia cycle[13–15]. Dexamethasone (DEX), a guideline-recommended glucocorticoid for severe pneumonia, carries risks of systemic immunosuppression, hyperglycaemia and delayed tissue repair[16,17]. Mechanical ventilation, although life-saving, can induce or exacerbate lung injury[18–20]. Antibiotics are effective only in infectious cases and offer no direct countermeasure against inflammation, oxidative stress, or hypoxia. Therefore, a modality that integrates antimicrobial, antioxidant, anti-inflammatory, and oxygen (O_2)-generating activities is urgently needed to break the ALI vicious cycle.

Insights from studies using native microalgae and their metabolites to treat mammalian diseases have inspired alternative approaches[21]. Specifically, Haematococcus pluvialis (Hae) is a green microalga that

naturally produces astaxanthin (AST), an antioxidant more potent than vitamin C or E, and generates O_2 via photosynthesis[22–25]. AST has been shown to alleviate oxidative stress and inflammation through multiple pathways, including activation of Nrf2 and inhibition of the NLRP3 inflammasome[26,27], and photosynthetic O_2 evolution has been exploited to counteract hypoxia in other disease models[28,29]. However, applying native Hae to ALI/ARDS has not yet been reported, which faces two fundamental barriers: the deep lung is lightless, and the pathological oxidative stress suppresses microalgal metabolism[30,31]. Previous microalgae-based disease therapies mainly rely on passive AST delivery or external illumination, limited by dose-dependent toxicity and poor deep-tissue penetration, respectively[32,33].

Here, we report an ROS-activated photosynthetic biosystem, Hae@CC, that reprograms the pathological microenvironment in both infectious and non-infectious ALI. By encapsulating the chemiluminescent peroxyoxalate CPPO and the fluorophore Cy5 within Hae (Fig. 1a), we construct a bioenergetic platform that exploits pathological H_2O_2 to generate CL via chemiluminescence resonance energy transfer (CRET) (Fig. 1b). This artificial light source drives endogenous Hae photosynthesis, producing local O_2 and AST. In murine models of both bacterial and LPS-induced ALI, a single aerosolised dose of Hae@CC not only eradicates bacteria but also re-engineers the immune-metabolic landscape by alleviating hypoxia, neutralizing ROS, and orchestrating macrophage polarization toward a tissue-repair phenotype, thereby disrupting the core pathogenic cycle of ALI and promoting comprehensive pulmonary recovery (Fig. 1c).

Results

Multi-dimensional characterization of the ALI lung microenvironment

To systematically dissect the pathological characteristics of ALI, this study utilized two public transcriptomic datasets: one comprised whole blood transcriptomes comparing patients with mechanical ventilation complicated by ALI and subjects receiving mechanical ventilation alone (GSE32707), and the other contained in vitro transcriptomic data of LPS-induced macrophages. These analyses reveal substantial dysregulation of numerous inflammation- and immunity-related genes in the ALI group compared with patients receiving routine mechanical ventilation. Gene Ontology (GO) enrichment analysis shows prominent enrichment of biological processes including immune response-regulating signaling, acute inflammatory response, cellular response to LPS, and oxidative stress. Meanwhile, ligand-receptor pathways governing macrophage recruitment and polarization are also significantly enriched, indicating tissue injury and immune activation within the ALI microenvironment. (**Fig. S1-S2**).

Next, we established a bacterial infection-induced murine ALI model and performed pulmonary microbiome profiling via 16S rRNA gene sequencing targeting the V2, V3, V5, V6 and V8 hypervariable regions. Principal component analysis (PCA) revealed a clear separation of microbial community

composition between healthy and ALI groups (Fig. 2a-2b), indicating a substantial alteration in community structure. Analysis at the phylum level revealed that the relative abundance of *Proteobacteria* (*Escherichia coli, E. coli*), the strain used for model construction in this study, belongs to it) was markedly elevated in the ALI group (**Fig. S3**), and further genus-level analysis demonstrated that the relative abundances of opportunistic pathogens (*Rhodopseudomonas*, *C1-B045*, and *Cyclobacteriaceae*) were significantly increased in the ALI group, whereas the abundances of homeostasis-related microbial taxa (*Kovelia*, *Marinobacter*, and *OM43_clade*) were notably reduced (**Fig. S4**)[34,35]. These observations indicate that pathogenic infection disrupts the pulmonary microbial ecosystem. To complement the microbial findings, we performed RNA sequencing on lung tissues from healthy and bacterial-induced ALI mice. We identified 2671 differentially expressed genes (DEGs, fold change > 2, false discovery rate [FDR] < 0.05), of which 1466 were upregulated and 1205 downregulated in the ALI group relative to controls (Fig. 2c). GO enrichment analysis of upregulated genes highlighted inflammatory (25 genes, P = 0.025) and immune (50 genes, P = 0.015) responses (Fig. 2d-e). Consistently, gene set enrichment analysis (GSEA) further revealed strong positive enrichment of inflammatory and immune response pathways in ALI samples (Fig. 2f-g). In addition, the cellular response to LPS showed significant positive enrichment in the ALI group (Fig. 2h). Collectively, these multi-omic data establish that the ALI microenvironment is characterized by robust inflammation activation, which drives macrophage recruitment and polarization, disrupts endothelial integrity and alters the pulmonary microbial ecosystem. These features provide a rationale for therapeutic strategies aimed at restoring immune-microbial homeostasis and suppressing excessive inflammation.

Rational design, preparation and characterization of Hae@CC

Hae possesses intrinsic O_2-generating capacity and synthesizes AST in a life-cycle-dependent manner[36]. Thus, Hae was first cultured under optimized conditions to ensure a metabolic state permissive for sustained O_2 evolution and AST biosynthesis (**Fig. S5**). CPPO and Cy5 were then co-encapsulated into cell-wall-deficient Hae to yield Hae@CC, an ROS-responsive photosynthetic biosystem, with loading efficiencies of approximately 65.2% and 22.7%, respectively (**Fig. S6–S7**). Spectral analysis confirmed the successful integration of both components, with the native spectral properties of CPPO and Cy5 preserved after encapsulation (Fig. 3a). Multicolor colocalization imaging revealed strong overlap between DiI-labeled Hae membranes and Cy5 fluorescence (tMr = 0.937, tMg = 0.942, ICQ = 0.462; Fig. 3b). Together, these data indicate that CPPO and Cy5 are efficiently co-encapsulated into cell-wall-deficient Hae with preserved optical properties.

Physicochemical characterization showed that Hae@CC exhibited a zeta potential of approximately −4.7 ± 0.3 mV (Fig. 3c) and a mean particle size of 21.8 ± 1.0 μm (Fig. 3d). The formulation remained stable in PBS containing 10% FBS at 4°C for 7 days, with no significant changes in size or zeta potential (Fig. 3e-f). Biocompatibility assessment by haemolysis assay revealed negligible haemolysis (< 0.6%) at concentrations up to 1×10^{10} cells/mL (Fig. 3g).

To probe the CRET mechanism, we added H_2O_2 to Hae@CC in the dark; the Cy5 emission spectrum became readily detectable, consistent with CPPO reacting with H_2O_2 to generate CL that excites Cy5 via CRET (Fig. 3h). Moreover, AST production in Hae@CC was substantially higher than that in unmodified Hae, CPPO-loaded Hae (Hae@CPPO), and Cy5-loaded Hae (Hae@Cy5) (Fig. 3i), suggesting that CRET-mediated photoactivation is associated with increased AST biosynthesis. These results support a CRET-mediated route for Hae@CC photoactivation and its association with enhanced AST production.

To further evaluate the ROS-responsive functionality, we compared Hae@CC with unmodified Hae, Hae@CPPO, and Hae@Cy5. After 30 min of H_2O_2 exposure, Hae@CC consumed the most H_2O_2, reducing the residual concentration to 35.5% of that in unmodified Hae, 37.7% of that in Hae@Cy5, and 72.9% of that in Hae@CPPO (Fig. 3j). Notably, under dark conditions in the presence of H_2O_2, Hae@CC exhibited the fastest O_2 generation rate and reached its O_2 production peak at 10 min (Fig. 3k), and it also yielded the maximum total O_2 output within 10 min. (**Fig. S8**). These results indicate that the complete Hae@CC system is required for effective ROS scavenging, O_2 evolution and AST biosynthesis.

Therapeutic effects of Hae@CC in vitro

Given the enrichment of potentially pathogenic bacteria, including *E. coli*, in the ALI microenvironment, we first evaluated the antibacterial activity of Hae@CC against *E. coli*, a common pathogen in bacterial-induced ALI[37]. Colony-forming unit (CFU) counts revealed that Hae@CC significantly reduced bacterial viability compared with PBS, decreasing from 1679 ± 187 CFU to 654 ± 142 CFU (Fig. 4a), an effect probably attributable to intrinsic antimicrobial metabolites derived from Hae[38,39]. Mechanistically, Hae@CC lowered bacterial ATP levels and increased surface zeta potential relative to PBS (Fig. 4b–c), suggesting disruption of membrane potential balance and inhibition of energy metabolism.

We next assessed the cytoprotective effect of Hae@CC on lung epithelial cells under inflammatory challenge with LPS. Live/Dead staining (Fig. 4d–e) and Annexin V-FITC/PI flow cytometry (Fig. 4f–g, **Fig. S9**) showed that LPS markedly increased the rate of A549 cell apoptosis, and the percentage of apoptotic cells rose from 4.9% in the control group (without LPS induction) to 12.9% in the LPS-treated group. Unmodified Hae moderately inhibited apoptosis, with the number of apoptotic cells comparable to that of the control group. In contrast, Hae@Cy5 and Hae@CPPO exhibited inferior protective effects, and the proportions of apoptotic cells only decreased to 7.5% and 5.9%, respectively. Notably, Hae@CC treatment resulted in the lowest apoptotic rate among all groups, and the number of apoptotic cells in the Hae@CC group reached only 5.2% and the anti-apoptotic effect was concentration-dependent (**Fig. S10**). Consistent with these findings, Hae@CC significantly promoted A549 cell proliferation, as evidenced by increased Ki67 expression (Fig. 4h-i).

To evaluate the tissue repair potential of Hae@CC, we performed wound-healing and tube-formation assays using human umbilical vein endothelial cells (HUVECs). By eliminating intrinsic H_2O_2 and continuously supplying O_2 to relieve basal oxidative stress and local hypoxia that hinder endothelial function, Hae@CC significantly enhanced the migratory capacity of HUVECs, achieving 1.8-fold increase

in wound-closure area relative to PBS, and outperforming unmodified Hae, Hae@Cy5 and Hae@CPPO by 1.5-fold, 1.4-fold and 1.3-fold, respectively (Fig. 4j–k). Consistently, in the tube-formation assay, Hae@CC showed the strongest pro-angiogenic activity, increasing the number of vascular junctions by 2.8-fold, 1.6-fold, 1.4-fold and 1.3-fold over the PBS, Hae, Hae@Cy5 and Hae@CPPO groups, respectively, owing to its dual ROS-scavenging and oxygen-generating functions (Fig. 4l–m).

Given the reported therapeutic potential of free AST in ALI and other inflammatory diseases[40], we compared free AST and Hae@CC in LPS-induced apoptosis and endothelial migration. Free AST partially inhibited A549 apoptosis and modestly promoted HUVEC migration. Hae@CC was more effective, reducing the percentage of apoptotic cells to 23.5% of that in the free AST group (**Fig. S11**) and increasing the migrated area to 2.1 times that of free AST-treated cells (**Fig. S12**). Together, these results show that Hae@CC exerts multifaceted effects, including antibacterial activity, protection against LPS-induced epithelial apoptosis, promotion of epithelial proliferation, and enhancement of endothelial migration and tube formation. Its intact ROS-responsive photosynthetic system outperforms free AST through sustained O_2 supply and in situ AST generation.

Anti-inflammatory and antioxidant properties of Hae@CC

The ALI microenvironment is characterized by excessive ROS production, which exacerbates tissue hypoxia and damage[12]. Hae@CC was designed to convert pathological ROS into O_2 and AST via CRET-driven photosynthesis, thereby alleviating hypoxia, inflammation, and oxidative stress injury and promoting macrophage polarization toward a reparative phenotype (Fig. 5a). For confirmation, we isolated murine bone marrow-derived macrophages (BMDMs) and stimulated them with LPS. Flow cytometry analysis revealed that LPS induced a high proportion of M1-type macrophages ($CD11b^+CD86^+$), whereas Hae@CC treatment significantly increased the proportion of M2-type macrophages ($CD11b^+CD206^+$) and decreased the M1 population (Fig. 5b-c, **Fig. S13**). Consequently, the M2/M1 ratio in the Hae@CC group was 4.2-fold that of the PBS group, 3.8-fold that of the Hae@Cy5 group, and 1.6-fold that of the Hae@CPPO group (Fig. 5d). Consistent with this phenotypic transition, Hae@CC induced the highest production of the anti-inflammatory cytokine TGF-β and significantly reduced pro-inflammatory cytokines TNF-α, IL-6 and IL-1β (Fig. 5e).

We next assessed the antioxidant capacity of Hae@CC in LPS-challenged A549 cells. Intracellular ROS levels, measured with DCFH-DA probe, showed that both Hae and Hae@Cy5 reduced ROS levels compared with PBS, an effect attributed to the antioxidant properties of AST (Fig. 5f). Notably, The Hae@CPPO and Hae@CC groups exhibited the strongest ROS scavenging capacity, reducing the ROS levels from 100% in the PBS group to 55.9% and 56.4%, respectively (**Fig. S14**). We next assessed the O_2-generating capability of Hae@CC under hypoxic conditions using the O_2-quenchable probe $Ru(dpp)_3$. The Hae@CC group showed the weakest fluorescence signal after 24 h of treatment, indicating the highest O_2 production (Fig. 5g). Accordingly, HIF-1α protein expression was significantly reduced in the Hae@CC-treated group (Fig. 5h). Collectively, these results demonstrate that Hae@CC works through a

self-sustaining loop. CRET-driven endogenous photosynthesis scavenges ROS, sustains Hae in O_2 and AST production, thereby alleviating hypoxia and exerting anti-inflammatory and antioxidant effects that collectively break the ALI cycle.

In vivo distribution and therapeutic effects of Hae@CC in LPS-induced ALI mice

We first confirmed that Hae@CC exhibited negligible cytotoxicity in vitro at concentrations up to 10^6 cells/mL (**Fig. S15**). To assess pulmonary delivery efficiency, we administered 50 μL of Hae@CC (2×10^5 cells/mL) intratracheally and monitored Cy5 fluorescence over time (Fig. 6a). Fluorescence signals peaked at 2 h and gradually declined by 20 h (Fig. 6b). Notably, over 25% of Hae@CC remained in the lungs 24 h after administration. Ex vivo lung imaging at 24 h revealed that fluorescence signals in the Hae@CC group were 1.3-fold stronger than those in the CPPO-Cy5 nanoparticles (CC-NPs) group (Fig. 6c–d), suggesting that incorporation of CPPO and Cy5 into Hae significantly prolongs pulmonary retention.

We next evaluated the therapeutic effect of Hae@CC in the LPS-induced ALI mouse model. Dose optimization showed that treatment with 2×10^5 cells/mL Hae@CC exerted the optimal therapeutic effect, with no detectable toxicity as assessed by serum biochemical indices (**Fig. S16**). Mice were then randomly divided into six groups and separately treated with PBS, Hae, Hae@Cy5, Hae@CPPO, Hae@CC (2×10^5 cells/mL,50μL) or DEX (0.5 mg/kg). Healthy mice receiving PBS served as the normal control. Macroscopic examination of lung tissues showed that Hae@CC treatment resulted in the greatest improvement, with normal lung color and texture and minimal dark lesions, then Hae@CC also effectively restored alveolar structure, reduced vascular permeability and edema, and lowered the lung wet-to-dry weight ratio (Fig. 6e-f**)**. By contrast, all other treatment groups exhibited varying degrees of lung damage. Hematoxylin-eosin (H&E) staining revealed severe alveolar damage with pronounced inflammatory infiltration in LPS-challenged mice, whereas Hae, Hae@Cy5, and Hae@CPPO groups exhibited only mild amelioration (Fig. 6g). Immunohistochemical analysis of Ki67 revealed that Hae@CC treatment promoted cell proliferation, outperforming even the DEX group (Fig. 6h).

Given the known pro-angiogenic capacity of microalgae[39], we next evaluated CD31 expression in lung sections by immunohistochemical (IHC) staining as a marker of vascular repair. Hae@CC treatment led to significantly higher CD31 levels than all other groups (Fig. 6i), supporting tissue remodelling and providing a structural basis for functional recovery[40]. Accordingly, pulmonary function parameters, including respiratory frequency, tidal volume, total lung volume and alveolar ventilation, were substantially improved in Hae@CC-treated mice (Fig. 6j). Together, these in vivo data demonstrate that Hae@CC exerts synergistic therapeutic effects, underscoring its potential as an effective platform for ALI management.

Therapeutic effects and mechanism of Hae@CC in bacteria-induced ALI mice

To extend our findings to an infectious setting, we evaluated Hae@CC in a murine model of *E. coli*-induced ALI. All Hae-based formulations significantly reduced bacterial loads in lung homogenates compared with PBS, with comparable antibacterial activity among them. The bacterial count in these groups was approximately 27.5% of that in the PBS group. Moreover, all Hae-based groups displayed superior antibacterial efficacy relative to the positive control DEX group, with CFU counts reaching roughly 32.4% of those in the DEX group (Fig. 7a-b).

We next examined macrophage polarization in lung tissues. Consistent with the in vitro findings, Hae@CC markedly promoted M2-type ($CD11b^+CD206^+$) over M1-type ($CD11b^+CD86^+$) macrophages. The M2/M1 ratio in the Hae@CC group was 3.8-fold, 2.4-fold, 2.3-fold, 1.6-fold and 1.7-fold that of the PBS, Hae, Hae@Cy5 Hae@CPPO and DEX groups, respectively (Fig. 7c-d, **Fig. S17**). We then assessed pulmonary capillary permeability by measuring total protein concentration in bronchoalveolar lavage fluid (BALF). Compared with the PBS group, the protein levels in the Hae, Hae@Cy5, and Hae@CPPO groups decreased to only 67.6%, 68.5%, and 68.4% of the PBS group, respectively. Notably, the Hae@CC group exhibited the best effect, with its total protein content reduced to approximately 31.2% of that in the PBS group, which was even superior to the DEX group (52.6%) and remained nearly consistent with the control group (Fig. 7e). Improved lung function was further reflected by enhanced oxyhemoglobin saturation, indicating alleviation of pulmonary hypoxia (Fig. 7f). Consistently, cytokine profiling revealed that Hae@CC markedly reduced the levels of pro-inflammatory cytokines (IL-6, IL-1β, TNF-α), which were comparable to those measured in healthy mice. In addition, anti-inflammatory cytokine TGF-β expression was increased by 3.8-fold, 2.5-fold, 2.7-fold and 2.9-fold higher than that of PBS, Hae, Hae@Cy5 and Hae@CPPO, respectively (Fig. 7g-j).

Finally, we assessed oxidative stress and tissue repair levels of Hae@CC in lung tissues. Immunostaining for GPX4 and HIF-1α, markers correlated with ROS and hypoxia, revealed markedly elevated levels in the model group, which were effectively reduced by Hae@CC (Fig. 7k-l). Collectively, these findings demonstrate that Hae@CC achieves synergistic anti-oxidative, anti-inflammatory and tissue-reparative effects, effectively breaking the infection-inflammation-hypoxia cycle in bacterial-induced ALI.

Discussion

In this study, we developed Hae@CC, a ROS-responsive photosynthetic biosystem, by co-encapsulating the chemiluminescent substrate CPPO and fluorophore Cy5 within cell-wall-deficient Hae. This system exploits pathological H_2O_2 in the ALI microenvironment to generate CL via CRET, which drives endogenous photosynthesis to produce O_2 and the antioxidant AST. By integrating antibacterial, antioxidant, anti-inflammatory and O_2-generating functions, Hae@CC effectively disrupts the self-

perpetuating cycle of infection, inflammation and hypoxia that underlies severe pneumonia and its subsequent ALI.

In both LPS- and bacteria-induced murine ALI models, intratracheal Hae@CC achieved sustained pulmonary retention and superior therapeutic outcomes, including reduced bacterial loads, restored alveolar architecture, decreased lung oedema, improved oxygenation and enhanced lung function. Mechanistically, Hae@CC promotes M1-to-M2 macrophage polarization, suppresses pro-inflammatory cytokines IL-1β, IL-6 and TNF-α, increases anti-inflammatory cytokines TGF-β expression, scavenges ROS, reduces HIF-1α expression and supports angiogenesis. Notably, Hae@CC outperformed DEX, the current guideline-recommended therapy, while avoiding the known side effects of corticosteroid treatment. These combined effects collectively drive lung tissue repair and functional recovery.

Several limitations remain. Long-term biodistribution, metabolic fate and immunogenicity require systematic evaluation, and the signalling pathways (for example, NF-κB, STAT3 and Nrf2) underlying macrophage polarization need further mechanistic clarification. Validation in clinically relevant multidrug-resistant strains and larger animal models, alongside dosing optimisation, will be needed for translation.

Our findings establish Hae@CC as a photosynthetic platform that addresses the infection–inflammation–hypoxia triad by harnessing pathological ROS, rather than external light, as an energy source. This work positions microenvironmental correction as a viable therapeutic strategy for acute inflammatory diseases characterized by local hypoxia and oxidative stress.

Methods

Materials and agents

4% paraformaldehyde (PFA, Cat: P1110), PBS buffer (Cat: P1020), Tris-HCl buffer (Cat: T1010), 30% acrylamide/bis solution (A1010), penicillin–streptomycin solution (Cat: P7630), 0.25% EDTA–trypsin (Cat: T1300), DCFH-DA (Cat: D6470), BSA-V (Cat: A8020), Tween-20 (Cat: IT9010), hydrogen peroxide assay kit (Cat: BC0205), BCA protein assay kit (Cat: PC0020), LPS (Cat: L8880), mouse TNF-α (Cat: SEKM-0034), IL-6 (Cat: SEKM-0007), TGF-β (Cat: SEKM-0035), IL-1β (Cat: SEKM-0002) ELISA kits, cellulase (Cat: C8270), pectinase (Cat: P8181), red blood cell lysis buffer (Cat: R1010), Hoechst 33342 (Cat: C0031), and Cy5 fluorescent dye (Cat: S1053) were purchased from Solarbio Science & Technology Co. Ltd. (Beijing, China). $Ru(dpp)_3$ assay kit (Cat: BES20583OD), ATP assay kit (Cat: S0027) and Live/Dead cell staining kit (Cat: ELS-ALX-850-249-KI01) were purchased from Beyotime. DMEM medium (Cat: 11965092), RPMI-1640 medium (Cat: 11875093), and fetal bovine serum (FBS) (Cat: A5670701) were purchased from Gibco (USA). Dexamethasone (Cat: D4902) was purchased from Sigma-Aldrich (USA). Astaxanthin ELISA (Cat: ml077076) was purchased from Shanghai Qiyuan Biotechnology (Shanghai, China). Goat anti-rabbit IgG (H + L) secondary antibody (Cat: 410406), rabbit anti-mouse CD86 antibody (Cat: 159219), rabbit anti-mouse CD206 antibody (Cat: 321118), and mouse CD11b antibody

(Cat: 101201) were purchased from BioLegend. HIF-1α antibody (Cat: ab51608) was purchased from Abcam. Matrigel matrix was purchased from Corning (Cambridge, UK).

Cell culture

Haematococcus pluvialis (Hae, NABRC FACHB-712) were collected by centrifugation at 1000 × g for 10 min. The cell pellets were washed 2–3 times with PBS and then treated with cellulase and pectinase (5 mg/mL) for cell wall digestion and removal.

Human umbilical cord mesenchymal stem cells (HUMSCs) were obtained from the Cell Resource Center, Peking Union Medical College, and cultured in complete HUMSC medium (SIMPSONLIFE, China). A549 cells and HUVECs were obtained from ATCC and cultured in high-glucose DMEM containing 10% FBS, penicillin (100 U/mL) and streptomycin (100 μg/mL) at 37°C in a 5% CO_2 atmosphere.

Transcriptome analysis

Mice (male, C57BL/6J, 6–8 weeks old) were subjected to a minimum 12-h fast prior to pulmonary administration to avoid suffocation or death caused by food residues retained in the buccal pouches, which could enter the trachea during intratracheal intubation or as a result of physiological unconditioned reflexes. Each mouse was weighed using a precision balance. An *Escherichia coli* (*E. coli*) suspension at 2 × 10^7 cells/mL was prepared in PBS. Mice were anesthetized via inhalation of veterinary isoflurane until respiration stabilized. Using a pulmonary delivery nebulizer, 50 μL of the bacterial suspension was intratracheally instilled into each mouse to ensure full delivery into the lung parenchyma and eliminate interference from coughing.

The dataset adopted in this study was GSE32707. Its microarray data were downloaded in MINiML format, which contains complete information regarding platforms, samples, and records.

Transcriptome sequencing was performed by LC-Bio Technologies Co., Ltd. (Hangzhou, China). The Subread package was used to calculate gene counts. RPKM and FPKM values were calculated based on gene length and mapped read counts. Differential expression analysis between two groups (six biological replicates per group) was performed using the DESeq2 R package (1.16.1), with P-values adjusted by the Benjamini–Hochberg method (adjusted $P < 0.05$ considered significant). GO and KEGG enrichment analyses were conducted using the R package clusterProfiler, employing both over-representation analysis (ORA) for differentially expressed genes and GSEA for all genes to identify significantly enriched pathways.

Optimization of the synergistic ratio of Hae with CPPO and Cy5

Purified Hae (1 × 10^6 cells/mL) were incubated with CPPO at indicated concentrations (4, 8, 12, 16, 20, 25, or 28 μg/mL) in a constant-temperature shaker (37°C, dark) for 1 h. After incubation, the mixtures were centrifuged at 800 × g for 5 min to remove unbound CPPO, yielding CPPO-loaded Hae. The CPPO loading content was determined by UV absorption spectroscopy (Thermo, Microplate Reader). Similarly,

purified Hae were incubated with Cy5 at concentrations of 4, 8, 16, 32, 64, or 128 μg/mL under the same conditions. After centrifugation, Cy5-loaded Hae were obtained, and the Cy5 loading content was determined by UV absorption spectrophotometry. Loading efficiency was calculated as:

Loading efficiency (%) = (Total mass of dye − Unbound dye mass) / Total mass of dye × 100%

The same formula was used for CPPO loading, with dye replaced by CPPO.

Colocalization imaging of Hae@CC

10 μL of Hae@CC (1×10^5 cells/mL) was dropped onto a poly-L-lysine (PLL)-coated glass slide. Cy5 fluorescence was excited at 640 nm (red channel), while Hae exhibited autofluorescence when excited at 430 nm. The colocalization efficiency was calculated using ImageJ.

Hemolysis assay of red blood cells

The blood compatibility of Hae@CC was assessed using a standard *in vitro* hemolysis assay. Fresh whole blood was collected and treated with anticoagulant. Red blood cells were washed three times with PBS at 3000 × g for 10 min and resuspended to prepare a red blood cell suspension, which was then mixed with 200 μL of Hae@CC (1×10^4, 1×10^5, 1×10^6, 1×10^7, 1×10^8, 1×10^9, or 1×10^{10} cells/mL) and incubated at 37°C for 12 h. After incubation, the absorbance of the supernatant was measured at 540 nm. The hemolysis rate was calculated according to the equation:

Hemolysis rate (%) = $(A_{sample} - A_{PBS}) / (A_{DI\ water} - A_{PBS}) \times 100\%$

Measurement of H_2O_2 consumption

The assay was performed according to the instructions of the hydrogen peroxide (H_2O_2) detection kit. Briefly, 1 mL of the H_2O_2 standard was added to Hae, Hae@Cy5, Hae@CPPO, or Hae@CC (1×10^6 cells/mL) for 30 min, then 250 μL samples were collected and mixed with 25 μL of reagent 2 and 50 μL of reagent 3. The mixture was centrifuged at 4000 × g for 10 min, and the supernatant was discarded. 250 μL of reagent 4 was added, and the samples were mixed for 5 min. The mixtures were then centrifuged at 800 × g for 5 min to remove the Hae cells. The supernatant was collected, and absorbance was measured at 415 nm using a microplate reader. The remaining concentration of H_2O_2 in each group was calculated based on the standard curve.

Antibacterial activity assay

Ampicillin-resistant *E. coli* (1×10^6 CFU/mL) were treated separately with PBS, Hae, Hae@Cy5, Hae@CPPO, or Hae@CC. After incubation for 48 h, the cultures were serially diluted 1,000-fold, plated on agar, and colonies were counted. To assess membrane surface charge, the bacterial suspensions were centrifuged at 800 × g for 5 min, and the supernatant was collected for zeta potential measurement using dynamic light scattering (DLS, Malvern Instruments, UK). For ATP determination, 1.5 mL of the bacterial suspension was centrifuged at 3000 × g for 5 min. The supernatant was discarded, and the pellet was resuspended in 200 μL of cell lysis buffer, mixed thoroughly, and incubated for 5 min. The

lysates were centrifuged at 12,000 × g for 5 min, and the supernatant was collected and kept on ice. ATP levels were quantified using a commercial ATP detection kit according to the manufacturer's instructions.

For the *in vivo* antibacterial activity assay, mice received intratracheal administration of PBS, Hae, Hae@Cy5, Hae@CPPO, Hae@CC (1×10^4 cells in 50 μL PBS) or by gavage administration of dexamethasone (0.5 mg/kg). Two hours later, mice were intratracheally infected with *E. coli* (1×10^6 CFU per mouse). After 24 h, lungs were harvested and homogenized into single-cell suspensions by passing through a 40-μm cell strainer. The resulting suspensions were serially diluted 1,000-fold, plated on agar, and bacterial colonies were counted.

Anti-apoptotic and pro-growth effects of Hae@CC

A549 cells were seeded in 6-well plates at a density of 1×10^6 cells per well. An inflammatory model was established by stimulating the cells with 1 μg/mL LPS for 12 h. Subsequently, cells were treated with PBS, Hae, Hae@Cy5, Hae@CPPO, or Hae@CC for 24 h. After treatment, the cells were digested with trypsin and stained with Calcein-AM/PI using a Live/Dead viability kit. For Ki67: cells were fixed with 4% paraformaldehyde. After permeabilization and blocking, the cells were incubated with Ki-67 primary antibody at 4°C overnight. After washing with PBST, fluorescent-conjugated secondary antibody was added and incubated at room temperature in the dark for 2 h. Fluorescence images were acquired with a laser scanning confocal microscope (CLSM, Nikon A1R, Japan).

Cell migration assay of Hae@CC

HUVECs were seeded into 6-well culture plates at a density of 2×10^6 cells/well and incubated until full confluence was achieved. A linear scratch was made across the center of each well, and the wells were washed three times with PBS to remove detached cells. Cells were then treated with PBS, Hae, Hae@Cy5, Hae@CPPO, or Hae@CC in high-glucose DMEM supplemented with 2% FBS for 24 h. After incubation, cells were imaged using an optical microscope, and the scratch closure area was quantified with ImageJ.

Angiogenesis assay of Hae@CC

Matrigel (Corning) was thawed at 4°C, diluted 10-fold, and 50 μL was added to each well of a 96-well plate. The plate was incubated at room temperature for 60 min to allow polymerization. HUVECs were seeded onto the Matrigel surface at a density of 1×10^3 cells/well. Cells were then treated with PBS, Hae, Hae@Cy5, Hae@CPPO, or Hae@CC (1×10^6 cells/mL). After incubation for 4 h at 37°C in a 5% CO_2 incubator, the wells were washed twice with PBS and imaged using an optical microscope. The formation of capillary-like tubular networks was quantified with ImageJ.

Cellular H_2O_2 consumption and ROS detection of Hae@CC

LPS-induced A549 cells (1×10^6 cells/mL) were treated with PBS, Hae, Hae@Cy5, Hae@CPPO, or Hae@CC (1×10^5 cells/mL, respectively) for 24 h. The cells were washed once with PBS, and then

incubated with Amplex Red reagent and 10 μL horseradish peroxidase (HRP) at 37°C for 30 min. Aliquots of 200 μL supernatant were transferred to a 96-well plate, and fluorescence was measured using a microplate reader (BioTek Synergy H1).

For intracellular ROS detection, A549 cells were seeded into glass-bottom confocal dishes (5×10^5 cells) and incubated overnight. After LPS stimulation to induce inflammation, cells were treated with different formulations for 24 h. Cells were then incubated with 500 μL of DCFH-DA solution (1:1000 dilution in serum-free medium) at 37°C for 20 min. After incubation, the cells were washed with serum-free medium to remove excess probe. ROS levels were visualized by confocal laser scanning microscopy (CLSM, Nikon A1R, Japan).

Polarization of macrophages by Hae@CC

Primary peritoneal macrophages isolated from mice were stimulated with LPS (150 ng/mL) for 48 h to induce M1 polarization. Subsequently, the cells were treated with PBS, Hae, Hae@Cy5, Hae@CPPO, or Hae@CC (1×10^5 cells/mL, respectively). Following 24 h of treatment, the cells were stained with antibodies against CD11b, CD86, and CD206, and analyzed by confocal laser scanning microscopy and flow cytometry. The culture supernatants were collected and centrifuged at 2000 × g for 10 min at 4°C. ELISA assays were performed to determine the levels of TNF-α, IL-6, TGF-β, and IL-1β.

In vivo metabolism and biodistribution of Hae@CC

50 μL of Hae@CC (2×10^5 cells/mL) was administered intratracheally to mice (male, C57BL/6J, 6–8 weeks old). Whole-body fluorescence imaging was performed at 0, 2, 6, 12, 24, and 48 h post-administration using a small-animal *in vivo* imaging system (IVIS, PerkinElmer, USA). At 48 h post-administration, mice were sacrificed, and the heart, liver, spleen, lungs, and kidneys were harvested for *ex vivo* organ imaging. Fluorescence intensity (average radiant efficiency of Cy5) was quantified using Living Image software.

In vivo therapeutic and prophylactic effect of Hae@CC

Mice (male, C57BL/6J, 6–8 weeks old) were randomly divided into seven groups (n = 6 per group). Group 1 (healthy control) received sham intratracheal administration. Groups 2–6 received intratracheal administration of PBS, Hae, Hae@Cy5, Hae@CPPO, or Hae@CC (2×10^5 cells/ml, 50 μL). Group 7 received dexamethasone (0.5 mg/kg) by gavage. Two hours later, groups 2–7 were intratracheally challenged with LPS (5 mg/kg). Lung function was assessed 24 h after LPS challenge (PFT, DSI Buxco, USA). Subsequently, mice were euthanized, and the lungs were harvested, washed with PBS, and photographed to document gross morphology. The harvested lungs were then fixed in 4% PFA, embedded in paraffin, and sectioned along the maximum transverse plane. Sections were stained with H&E for histopathological analysis and immunohistochemically stained with antibodies against Ki67, HIF-1α, and CD31. ROS levels were assessed by corresponding fluorescence staining. For total protein measurement in mouse bronchoalveolar lavage fluid (BALF), BALF was collected, and the total protein

concentration was determined using a BCA protein assay kit according to the manufacturer's instructions. For lung wet-to-dry weight ratio determination, the lungs were dried at 37°C for 48 h and reweighed to determine the dry weight.

Statistical analysis

All data are presented as mean ± SD. Statistical significance was determined by one-way ANOVA with Šidák's multiple comparisons test. Significance levels are denoted as n.s. (not significant), *P < 0.05, **P < 0.01, ***P < 0.001, and ****P < 0.0001.

Data availability

All data supporting the findings of this study are available within the article and its supplementary files. Any additional requests for information can be directed to and will be fulfilled by the corresponding authors. Source data are provided with this paper.

Declarations

All animal experiments were approved by the Ethics Committee of Beijing Institute of Technology and performed under its oversight (approval ID: 2022-0009-138).

References

1. Martin-Loeches I, Reyes LF, Nseir S et al (2023) European Network for ICU-Related Respiratory Infections (ENIRRIs): a multinational, prospective, cohort study of nosocomial LRTI. Intensive Care Med 49:1212–1222
2. Alves D, Grainha T, Pereira MO et al (2023) Antimicrobial materials for endotracheal tubes: A review on the last two decades of technological progress. Acta Biomater 158:32–55
3. Barnes M, Feit C, Grant TA et al (2019) Antimicrobial polymer modifications to reduce microbial bioburden on endotracheal tubes and ventilator-associated pneumonia. Acta Biomater 91:220–234
4. Vincent JL, de Souza Barros D, Cianferoni S (2010) Diagnosis, management and prevention of ventilator-associated pneumonia: an update. Drugs 70:1927–1944
5. Long ME, Mallampalli RK, Horowitz JC (2022) Pathogenesis of pneumonia and acute lung injury. Clin Sci 136:747–769
6. Howroyd F, Chacko C, MacDuff A et al (2024) Ventilator-associated pneumonia: pathobiological heterogeneity and diagnostic challenges. Nat Commun 15:6447
7. Garcia IM, Rodrigues SB, Gama MER et al (2020) Guanidine derivative inhibits C. albicans biofilm growth on denture liner without promoting loss of materials' resistance. Bioact Mater 5:228–232
8. Wu YY, Zhang WN, Jiang YC et al (2026) Inhaled formulations for bacterial pneumonia: Strategies and advances in drug delivery. Bioact Mater 63:1–30

9. Chen X, Ling X, Liu G et al (2022) Antimicrobial Coating: Tracheal Tube Application. Int J Nanomed 17:1483–1494
10. Liu X, Boyer MA, Holmgren AM et al (2020) Legionella-Infected Macrophages Engage the Alveolar Epithelium to Metabolically Reprogram Myeloid Cells and Promote Antibacterial Inflammation. Cell Host Microbe 28:683–698
11. Asano K, Takahashi N, Ushiki M et al (2015) Intestinal CD169(+) macrophages initiate mucosal inflammation by secreting CCL8 that recruits inflammatory monocytes. Nat Commun 6:7802
12. Su F, Zhang C, Zhang Q et al (2025) Multifaceted Immunomodulatory Nanocomplexes Target Neutrophilic-ROS Inflammation in Acute Lung Injury. Adv Sci 12:e2411823
13. Qiao Q, Liu X, Yang T et al (2021) Nanomedicine for acute respiratory distress syndrome: The latest application, targeting strategy, and rational design. Acta Pharm Sin B 11:3060–3091
14. Levy SB, Marshall B (2004) Antibacterial resistance worldwide: causes, challenges and responses. Nat Med 10:122–129
15. Li H, Yuan Y, Zhang L et al (2024) Reprogramming Macrophage Polarization, Depleting ROS by Astaxanthin and Thioketal-Containing Polymers Delivering Rapamycin for Osteoarthritis Treatment. Adv Sci 11:e2305363
16. Wang X, Zhai J, Fan X et al (2025) Nanozyme antibiotic dressings to accelerate wound healing through anti-inflammatory and antibacterial effects. Mater Today Bio 36:102745
17. Auger JP, Zimmermann M, Faas M et al (2024) Metabolic rewiring promotes anti-inflammatory effects of glucocorticoids. Nature 629:184–192
18. Czuppon P, Day T, Débarre F et al (2023) A stochastic analysis of the interplay between antibiotic dose, mode of action, and bacterial competition in the evolution of antibiotic resistance. PLoS Comput Biol 19:e1011364
19. Goligher E, Ferguson N, Brochard L (2016) Clinical challenges in mechanical ventilation. Lancet 387:1856–1866
20. Slutsky AS, Ranieri VM (2014) Ventilator-induced lung injury. N Engl J Med 370:980
21. Leong DTL, Xing K et al (2026) Transplantation of plant photosynthetic light-reaction systems for energy and redox homeostasis in mammalian disease therapy. Cell 14:189
22. Luo R, Liu J, Dai L et al (2026) Stress-trained microalgae robots with probiotics backpack and intestinal brake for inflammatory bowel disease management. Nat Commun 17:173
23. Kang Y, Xu L, Dong J et al (2024) Programmed microalgae-gel promotes chronic wound healing in diabetes. Nat Commun 15:1042
24. Li X, Wang X, Duan C et al (2020) Biotechnological production of astaxanthin from the microalga Haematococcus pluvialis. Biotechnol Adv 43:107602
25. Dong J, Cheng BY, Zhang XN et al (2026) Microalgae extracellular vesicles-loaded dual antioxidative and anti-inflammatory hydrogel system for wound healing and peripheral nerve repair in diabetes. Bioact Mater 64:193–211

26. Zhang SM, Hu WX, Zhao YZ et al (2025) Bidirectional modulation of glycolysis using a multifunctional nanocomposite hydrogel promotes bone fracture healing in type 2 diabetes mellitus. Bioact Mater 50:152–170
27. Cai X, Hua S, Deng J et al (2022) Astaxanthin activated the Nrf2/HO-1 pathway to enhance autophagy and inhibit ferroptosis, ameliorating acetaminophen-induced liver injury. ACS Appl Mater Interfaces 14:42887–42903
28. Wang J, Li H, Su Q et al (2025) Living photosynthetic micro/nano-platforms: Engineering unicellular algae for biomedical applications. Bioact Mater 51:575–597
29. Lu S, Feng W, Dong C et al (2022) Photosynthetic oxygenation-augmented sonodynamic nanotherapy of hypoxic tumors. Adv Healthc Mater 11:e2102135
30. Liang F, Zheng Y, Zhao C et al (2025) Microalgae-derived extracellular vesicles synergize with herbal hydrogel for energy homeostasis in osteoarthritis treatment. ACS Nano 19:8040–8057
31. Wang R, Tong A, Jin K et al (2026) Harnessing the gut–immune–joint axis: Oral microalgae-based thermoresponsive microspheres enhance intra-articular therapy for rheumatoid arthritis. Bioact Mater 61:72–91
32. Wang R, Wang Z, Zhang M et al (2025) Application of photosensitive microalgae in targeted tumor therapy. Adv Drug Deliv Rev 219:115519
33. Celi N, Gong D, Cai J et al (2025) AlgaeSperm: Microalgae-based soft magnetic microrobots for targeted tumor treatment. Small 21:e2407585
34. Díaz-Marugan L, Gallizioli M, Márquez-Kisinousky L et al (2023) Poststroke Lung Infection by Opportunistic Commensal Bacteria Is Not Mediated by Their Expansion in the Gut Microbiota. Stroke 54:1875–1887
35. Perdijk O, Azzoni R, Marsland BJ (2024) The microbiome: an integral player in immune homeostasis and inflammation in the respiratory tract. Physiol Rev 104:835–879
36. Cui H, Zhu X, Yu X et al (2025) Advancements of astaxanthin production in Haematococcus pluvialis: Update insight and way forward. Biotechnol Adv 79:108519
37. Zou P, Huang L, Li Y et al (2024) Phase-Separated Nano-Antibiotics Enhanced Survival in Multidrug-Resistant Escherichia coli Sepsis by Precise Periplasmic EcDsbA Targeting. Adv Mater 36:e2407152
38. Yao L, Tao Q, Xian F, Chen Z, Huang L, Zhong N, Gao J (2025) Development of pullulan/gellan gum films loaded with astaxanthin nanoemulsion for enhanced strawberry preservation. Food Res Int 201:115644
39. Xing X, Liu C, Zheng L (2025) Preparation of photo-crosslinked microalgae-carboxymethyl chitosan composite hydrogels for enhanced wound healing. Carbohydr Polym 348:122803
40. Teng XN, Wang H, Zhu Y, Wang SC, Pan RL, Du C, Song RF, Zhang SS, Li JR, Zhang SB, Xu F, Zhang Q, Zhang M (2026) Astaxanthin-metformin conjugate nanomicelles-loaded hydrogel reprograms macrophage metabolism via mitochondrion-targeted regulation for diabetic wound healing. Bioact Mater 64:763–780

Figures

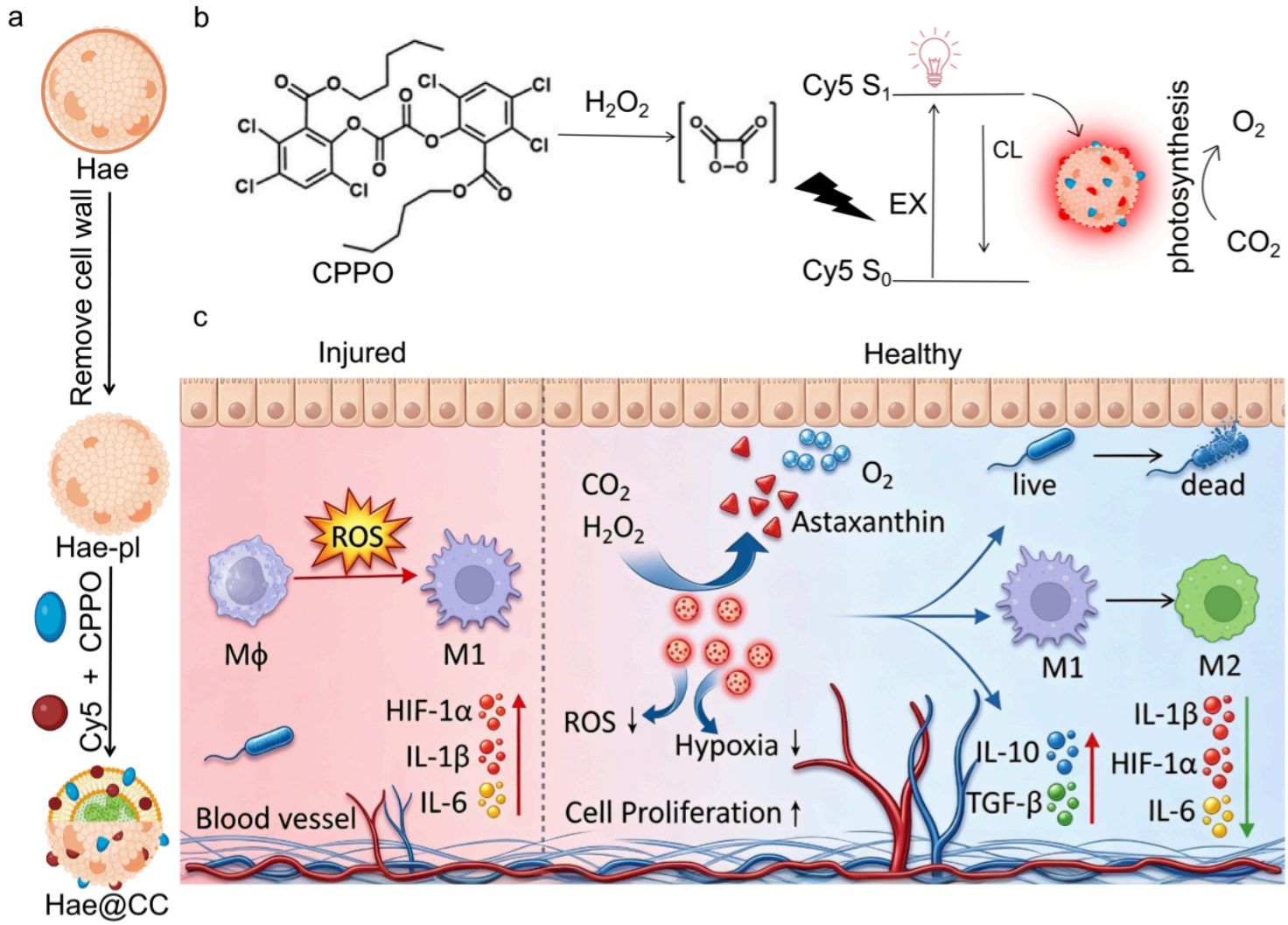


Figure 1

Schematic illustration of Hae@CC preparation and its therapeutic mechanism against bacterial pneumonia. a. Construction of Hae@CC. **b.** Endogenous photosynthesis of Hae@CC. **c**. Treatment mechanism of Hae@CC.

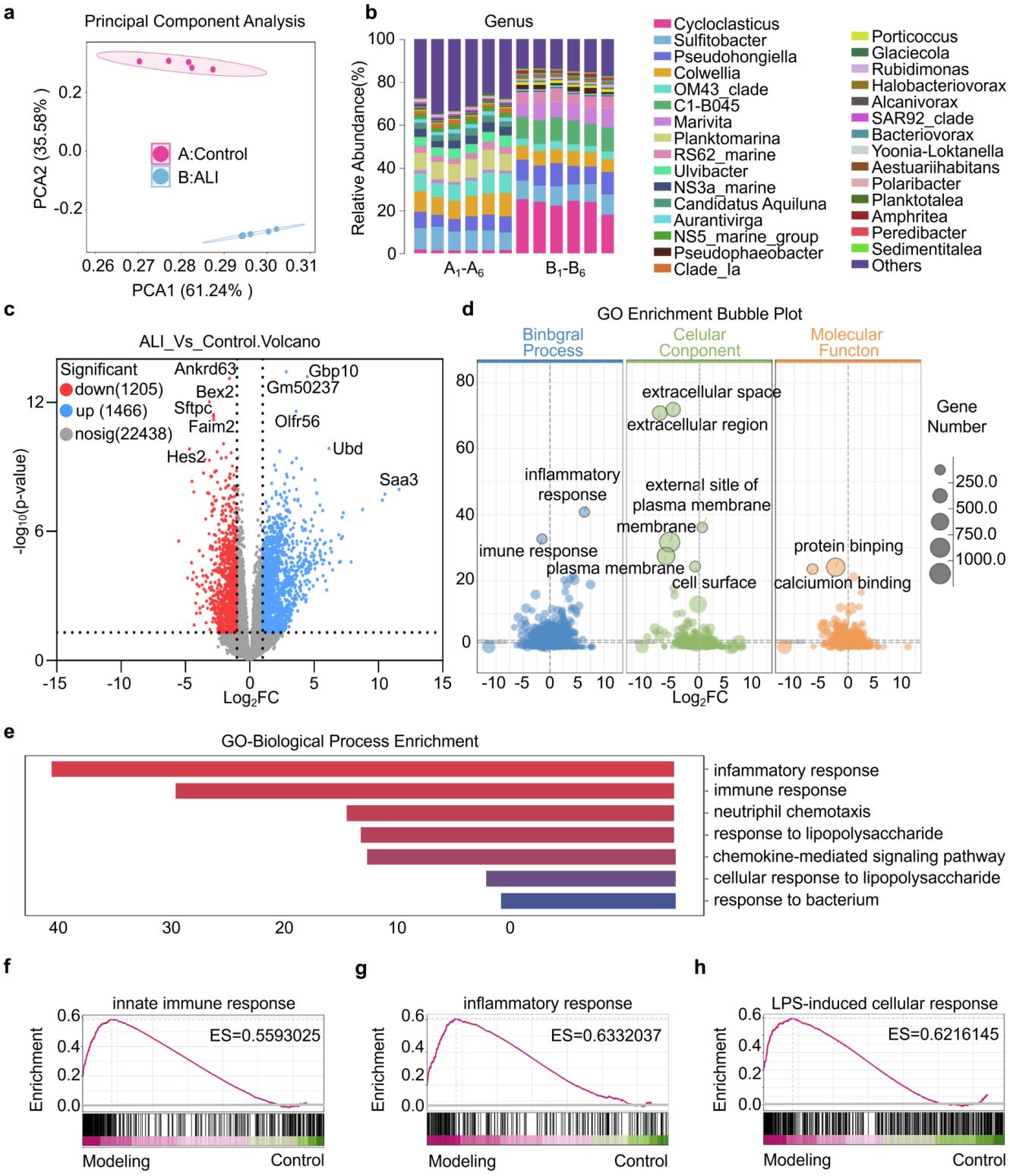


Figure 2

Landscape of pulmonary microbial dysbiosis and inflammatory signatures in ALI. a. PCA plot of 16S rRNA sequencing data from the lung tissue of healthy and *E. coli*-induced ALI mice. **b.** Stacked bar chart depicting the relative abundance of microbial taxa at the genus level. **c.**Volcano plot of DEGs from RNA-seq (fold change >2, FDR <0.05). **d-e.**GO enrichment analysis (d) and biological process enrichment (e) of upregulated genes displaying top enriched terms. **f-h.** GSEA results for innate immune response

(f), inflammatory response (g), and cellular response to LPS-induced cellular response (h) between the ALI group and healthy control group.

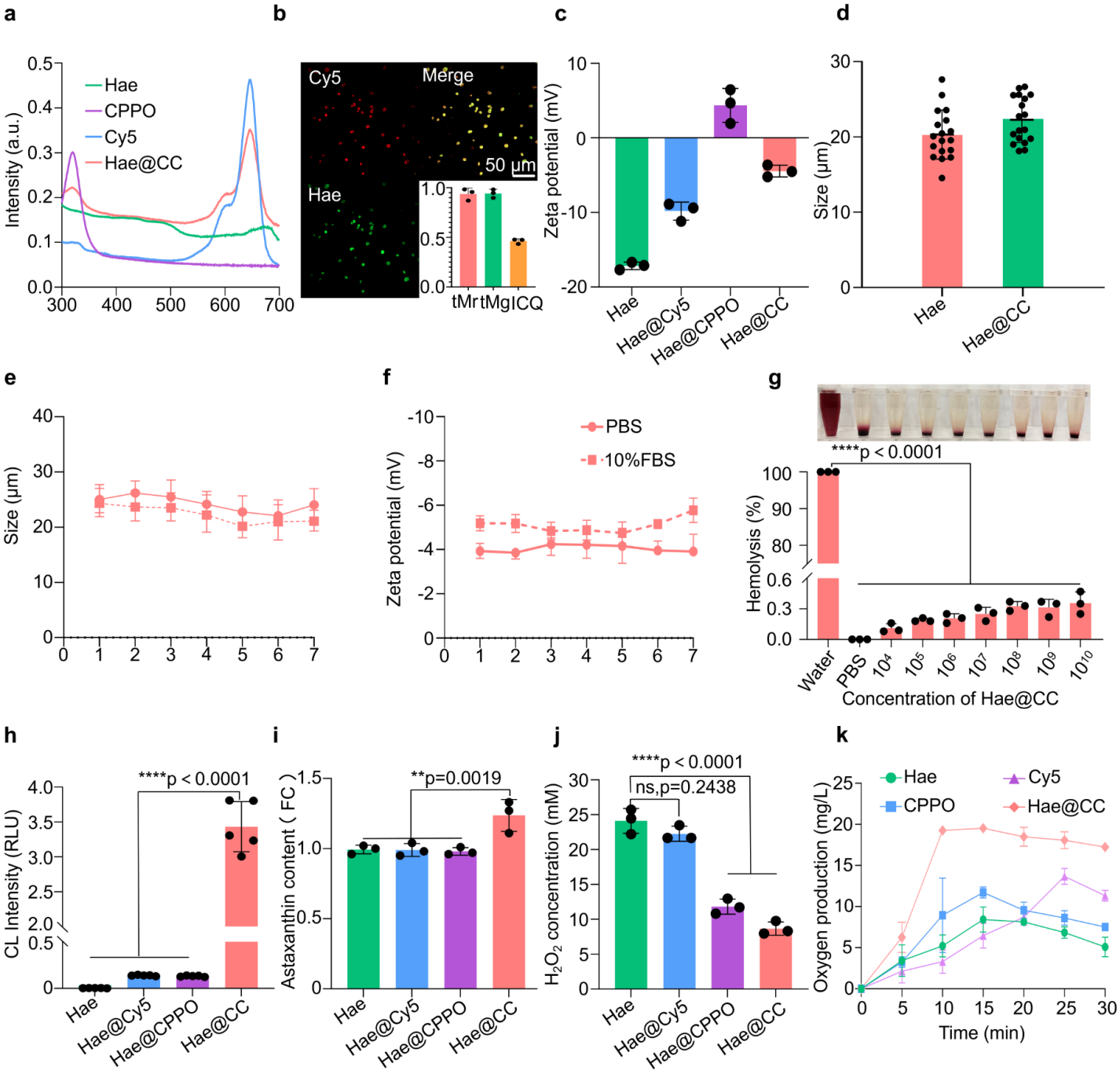


Figure 3

Preparation and characterization of Hae@CC. a. UV-vis absorption and fluorescence (FL) spectra of different formulations. **b.**Co-localization imaging of Cy5 (red) and Hae (green) in Hae@CC (Manders' coefficient, tMr for red channel, tMg for green channel; ICQ, intensity correlation quotient, n=3 independent samples). **c-d.** Zeta potential (c) and size distribution (d) of different formulations measured by dynamic light scattering (DLS) (For zeta potential n=3 independent samples, for size n=20

independent samples). **e-f.** Stability of Hae@CC in PBS or PBS containing 10% FBS over 7 days, assessed by changes in particle size (e) and zeta potential (f) (n=3 independent samples). **g.** Haemolysis assay of Hae@CC at indicated concentrations in PBS (n=3 independent samples). **h.** CL intensity of Cy5 triggered by CPPO-H_2O_2 reaction in dark(n=5 independent samples). **i.** Relative AST content in Hae after 7 days of culture (n=3 independent samples). **j-k.** H_2O_2 consumption efficiency (j) and O_2 generation (k) of different formulations in the presence of 1 mM H_2O_2 under dark conditions (n=3 independent samples). Data are means ± SD. Statistical significance was determined by one-way ANOVA with Sidak's multiple comparisons test; ns, not significant; ***P < 0.001; ****P < 0.0001.

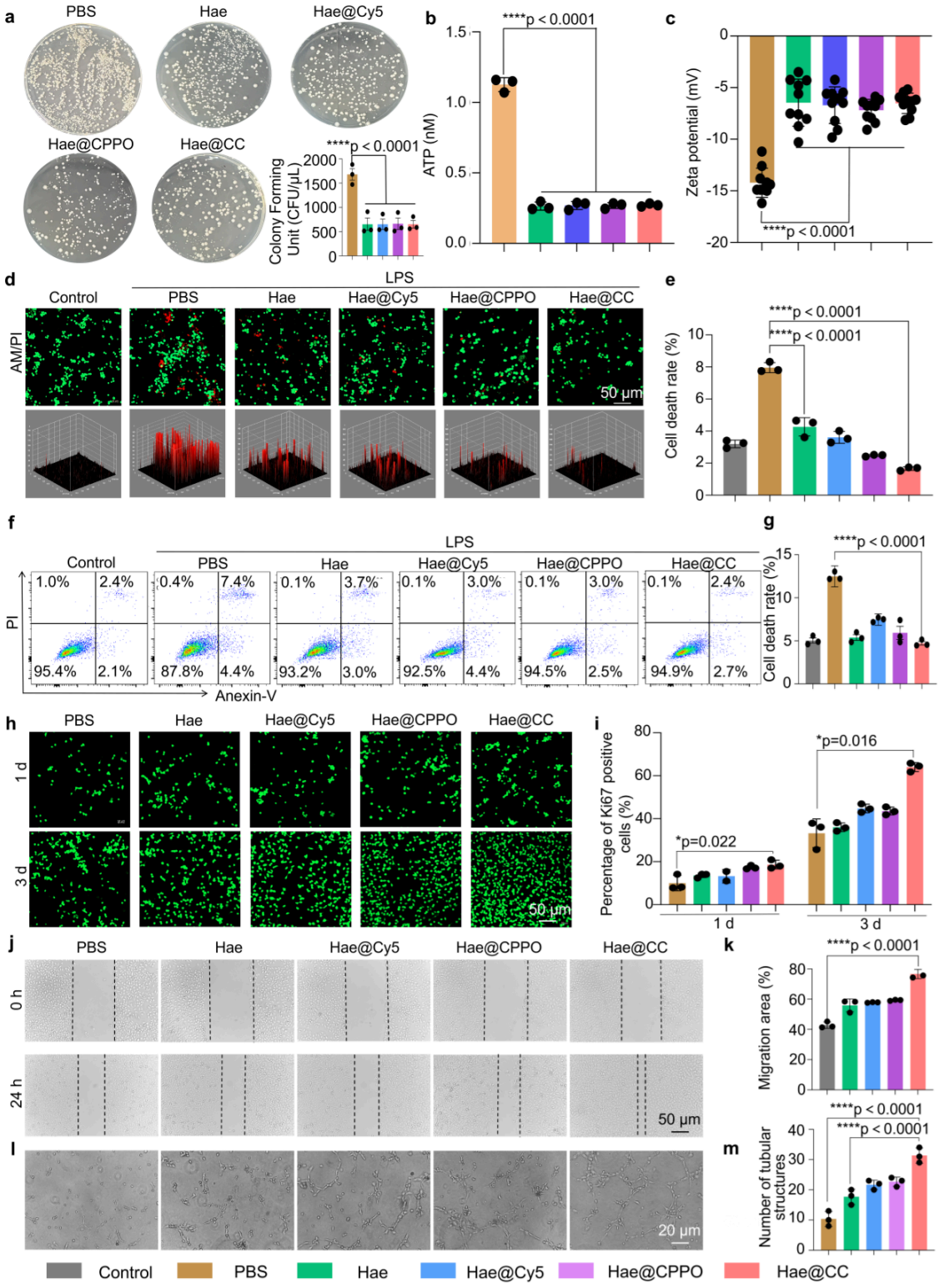


Figure 4

In vitro antibacterial, epithelial repair and pro-angiogenic activities of Hae@CC. a. Representative images of *E. coli DH5α* colonies after 48 h treatment (left) and quantification of CFU (right) (n=3 independent samples). **b.** ATP levels of bacteria treated as in (a) (n=3 independent samples). **c.** ζ-potential of *E. coli DH5α* under different treatments (n=10 independent samples). **d-e**, Representative confocal microscopy images (d) and quantification (e) of Live/Dead staining of A549 cells (green, live

cells; red, dead cells) (n=3 independent samples). **f-g**, Representative flow cytometry plots (f) and quantification (g) of Annexin V-FITC/PI staining of A549 cells (n = 3 independent samples). **h-i**, Representative images (h) and quantification (i) of Ki67 expression in A549 cells (n=3 independent samples). **j-k.**Representative images (j) and quantification of migration area (k) after 24 h in wound-healing assays (n = 3 independent samples). **l-m.** Representative images (l) and quantification (m) of tube formation assay using HUVECs after 24 h (n=3 independent samples). Data are means ± SD. Statistical significance was determined by one-way ANOVA with Sidak's multiple comparisons test; ns, not significant; *P < 0.05; **P < 0.01; ***P < 0.001; ****P < 0.0001.

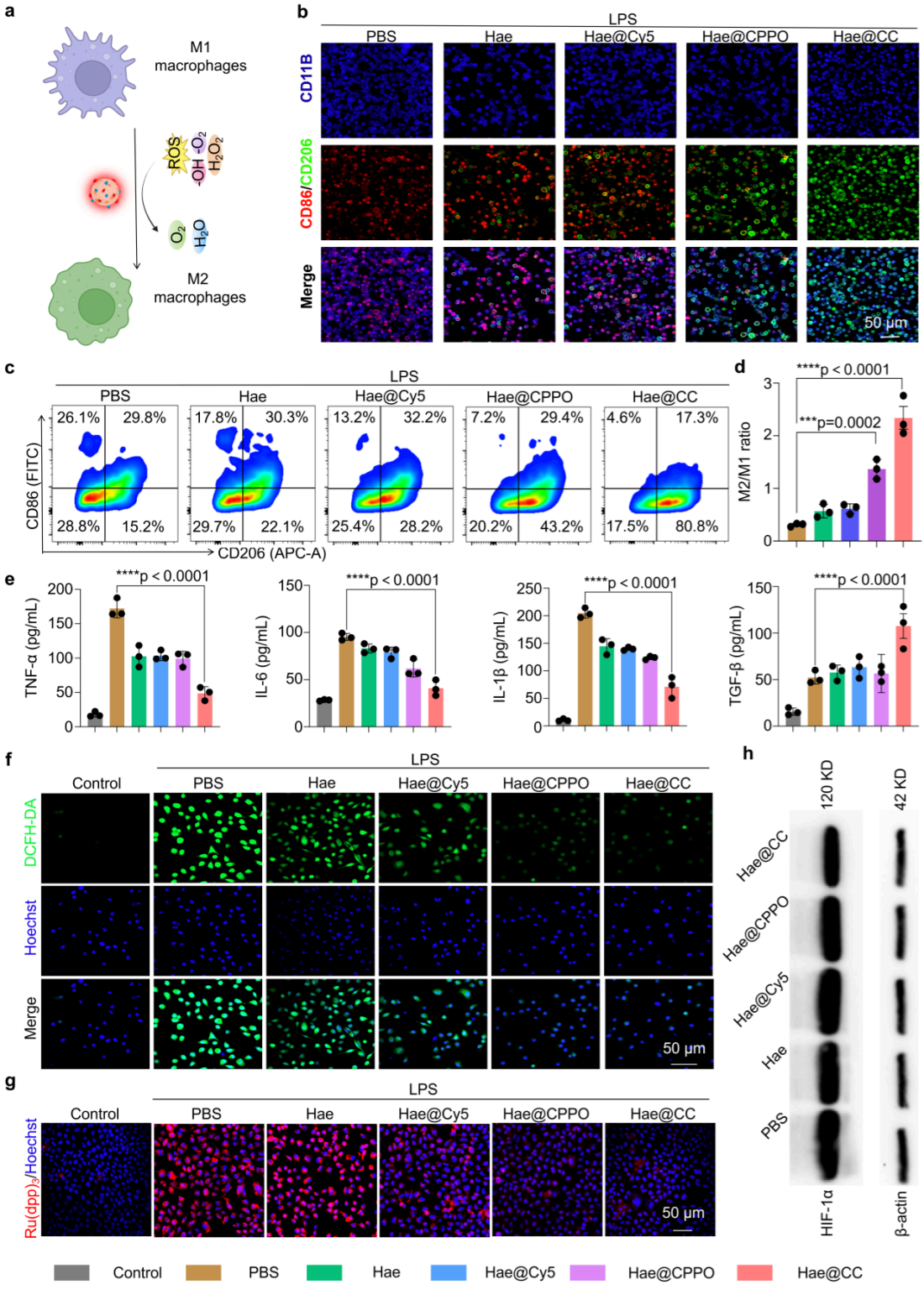


Figure 5

Anti-inflammatory and antioxidant properties of Hae@CC. a. Schematic illustration of the mechanism by which Hae@CC promotes M1-to-M2 macrophage polarization. **b.** Representative immunofluorescence images of macrophage phenotypes after different treatments. **c-d.** Flow cytometric analysis (c) and quantification (d) of M2/M1 macrophage ratio (n=3 independent samples). **e.** Cytokine (TGF-β, TNF-α, IL-6, IL-1β) release from BMDM supernatants after 48 h of co-culture with

different formulations (n=3 independent samples). **f.** Intracellular ROS levels in LPS-induced A549 cells after 24 h of treatment. **g.** O_2 generation assessed by $Ru(dpp)_3$ probe under hypoxic conditions. **h.** Western blot analysis of HIF-1α protein expression in A549 cells exposed to anaerobic conditions for 8 h of treatment. Data are means ± SD. Statistical significance was determined by one-way ANOVA with Sidak's multiple comparisons test; ns, not significant; ***P < 0.001; ****P < 0.0001.

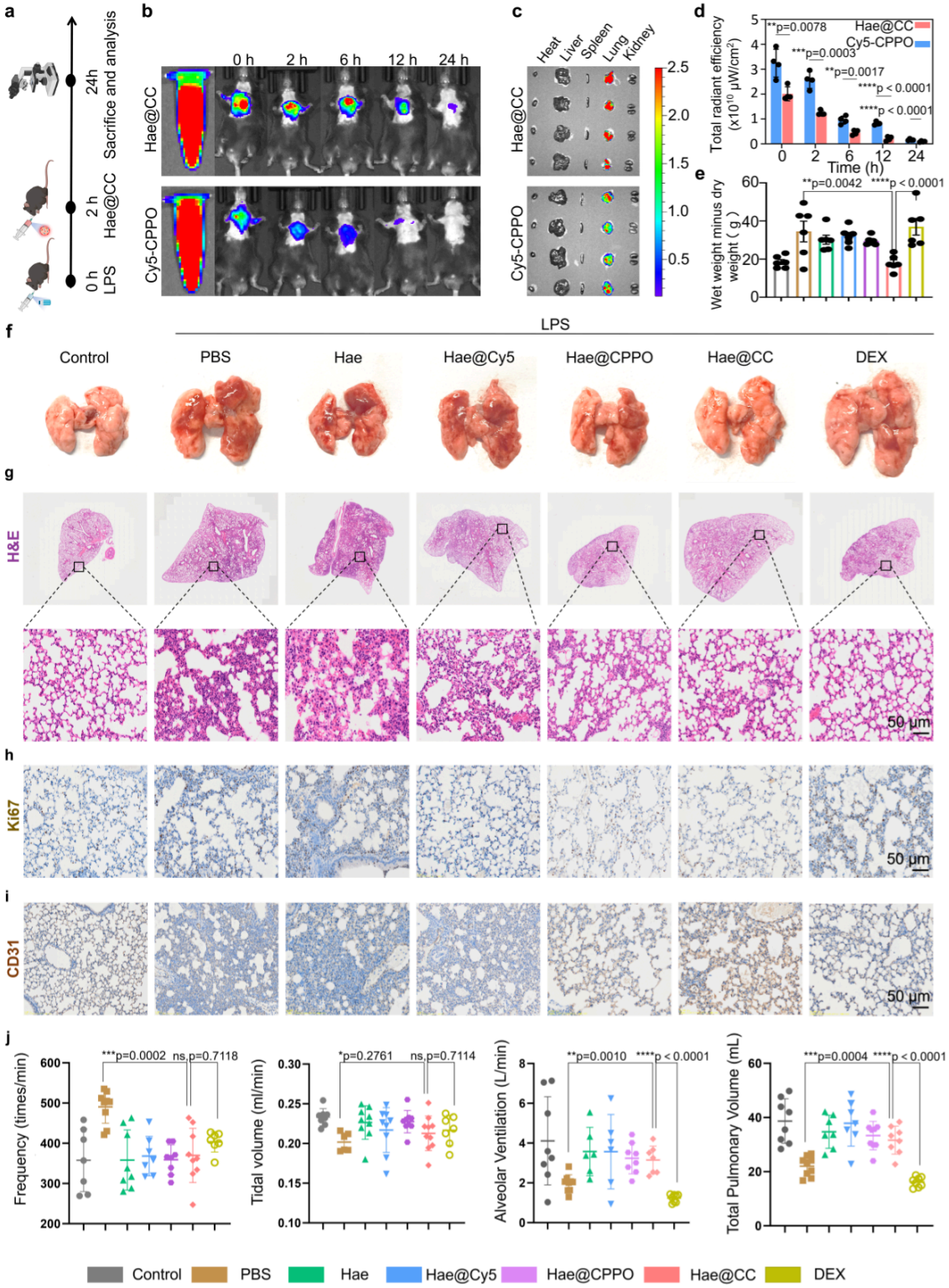


Figure 6

In vivo distribution and therapeutic effects of Hae@CC in LPS-induced ALI mice. a. Schematic illustration of the animal experimental procedure. **b.** In vivo imaging of Cy5 fluorescence in ALI mice at indicated time points after intratracheal administration of Hae@CC or CC-NPs. **c.**Ex vivo imaging of major organs (heart, liver, spleen, lung, kidneys) harvested at 24 h post-administration. **d.** Quantitative analysis of Cy5 fluorescence in lungs over time (n=4 independent samples). **e.** Lung wet weight minus dry weight of mice after indicated treatments (n=6 independent samples). **f.** Representative images of lung tissues from mice subjected to different treatments. **g-h.** H&E staining (g) and Ki67 IHCstaining (h) of lung sections. **i.** IHC analysis of CD31 expression in lung sections. **j.** Measurements of pulmonary function parameters including respiratory frequency, tidal volume, alveolar ventilation, total lung capacity (n=8 independent samples). Data are means ± SD. Statistical significance was determined by one-way ANOVA with Sidak's multiple comparisons test; ns, not significant; *P< 0.05; **P< 0.01.

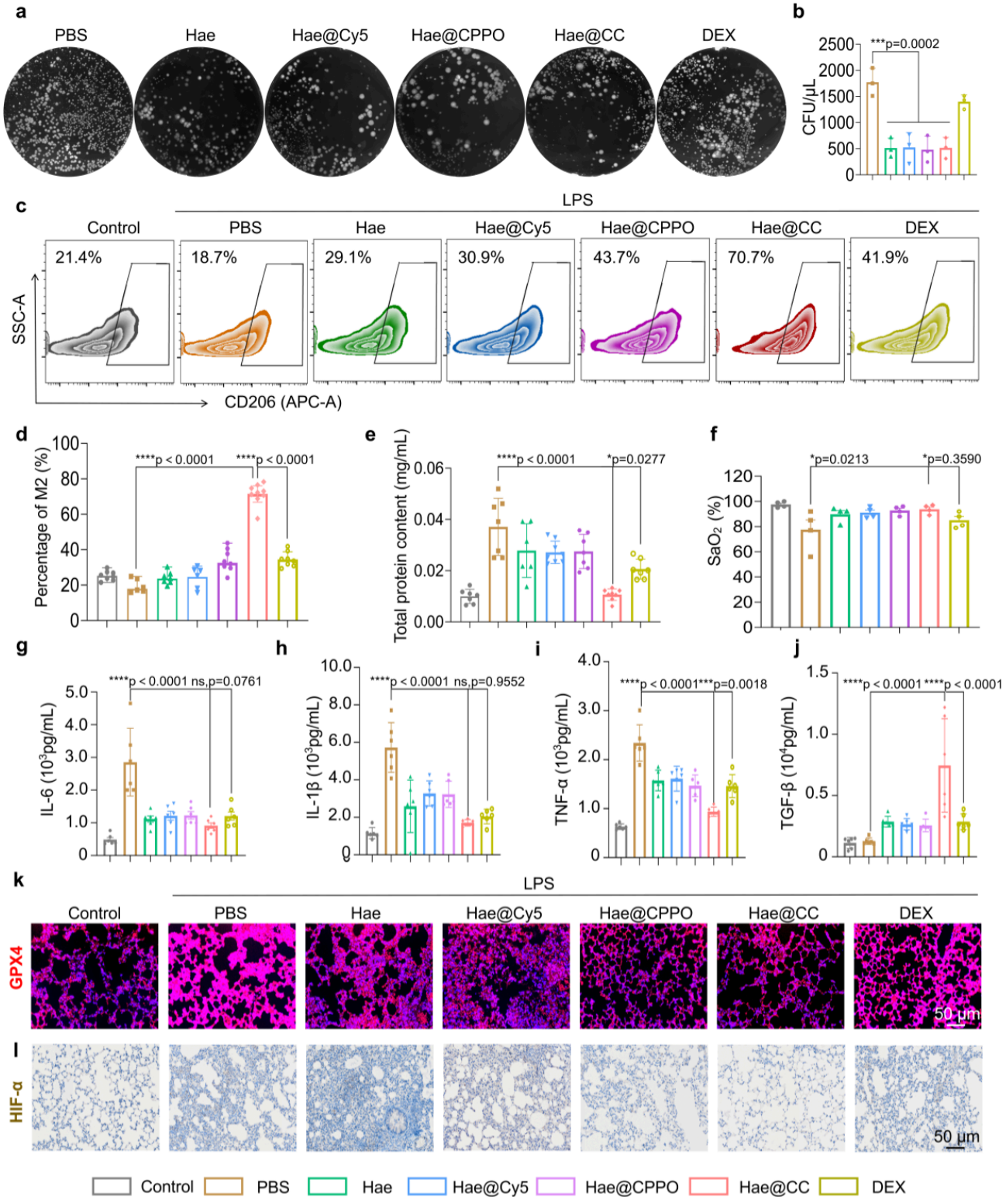


Figure 7

In vivo antibacterial, anti-inflammatory, and antioxidant effects of Hae@CC in a bacterial-induced ALI mouse model. a-b. CFU counts of *E. coli DH5α* in lung homogenates after 24 h treatment (n=3 independent samples). **c-d.**Flow cytometric analysis (c) and quantification of M2/M1 macrophage ratio (d) (M1: $CD11b^+CD86^+$; M2: $CD11b^+CD206^+$) (n=8 independent samples). **e.** Total protein concentration in BALF measured by bicinchoninic acid (BCA) assay (n=7 independent samples). **f.** O_2 saturation (SaO_2,

%) in mice after treatment with indicated formulations (n=4 independent samples). **g-j.** Expression levels of pro-inflammatory cytokines IL-6 (g), IL-1β (h), TNF-α (i), and anti-inflammatory cytokine TGF-β (j) in lung tissue, quantified by ELISA (n=6 independent samples). **k-l.** IHC analysis of GPX4 (k) and HIF-1α (l) expression in lung sections. Data are presented as mean ± SD. Statistical significance was determined by one-way ANOVA with Sidak's multiple comparisons test; ns, not significant; *P< 0.05; ***P< 0.001; ****P< 0.0001.

Supplementary Files

This is a list of supplementary files associated with this preprint. Click to download.

- figS20261001.docx
- SourceData.xlsx
- SupplementaryInformation.docx